

WavePlanes: A compact Wavelet representation for Dynamic Neural Radiance Fields

Adrian Azzarelli¹, Nentheera Anantrasirichai¹, and David R Bull¹

Visual Information Laboratory, University of Bristol,
a.azzarelli,n.anantrasirichai,dave.bull@bristol.ac.uk

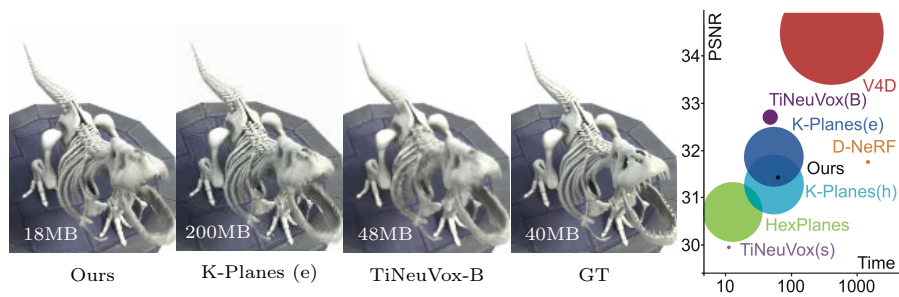


Fig. 1: **Left:** Visual comparison of state of the art Dynamic NeRFs. **Right:** Quantitative comparison of model size (point radius), training time (x-axis) and quality (y-axis)

Abstract. Dynamic Neural Radiance Fields (Dynamic NeRF) enhance NeRF technology to model moving scenes. However, they are resource intensive and challenging to compress. To address these issues, this paper presents WavePlanes, a fast and more compact explicit model. We propose a multi-scale space and space-time feature plane representation using N-level 2-D wavelet coefficients. The inverse discrete wavelet transform reconstructs feature signals at varying detail, which are linearly decoded to approximate the color and density of volumes in a 4-D grid. Exploiting the sparsity of wavelet coefficients, we compress the model using a Hash Map containing only non-zero coefficients and their locations on each plane. Compared to the state-of-the-art (SotA) plane-based models, WavePlanes is up to 15× smaller while being less resource demanding and competitive in performance and training time. Compared to other small SotA models WavePlanes preserves details better without requiring custom CUDA code or high performance computing resources. Our code is available at: <https://github.com/...>

Keywords: Neural Radiance Fields · Wavelets · Compression

1 Introduction

Neural Radiance Fields (NeRFs) have gained significant attention due to their ability to generate 3D scenes with accurate novel view synthesis. The traditional NeRF is designed for static scenes and struggles to model objects and scenes with motion. Dynamic NeRFs address the issue by modelling an additional time component to support the generation of realistic object and scene animations. While static NeRF frameworks yield impressive results, dynamic NeRF frameworks still face limitations with computational complexity, scalability and compression.

Recent advancements in plane-based representations, including matrix-vector and plane decomposed 3-D space, have demonstrated promising results for static scenes [5, 12, 22] and dynamic scenes [3, 8, 21], demonstrating substantial improvements to training speed. However, the significance and interpretability of the temporal component (typically represented by an axis along a 2-D grid $\in \{xt, yt, zt\}$) have not been fully realized, leading to a temporal loss in visual quality. Moreover, though faster in training, these models tend to be large, computationally costly and challenging to compress, making tasks such as file-sharing and streaming problematic. For static scenes, the masked wavelet-based tri-plane (MWT) representation has been proposed to resolve these issues [19]; unfortunately, applying them to dynamic scenes is not straightforward.

In this paper, we propose a novel dynamic plane representation and compression method for dynamic NeRF scenes. We use wavelets as a base representation to reduce computation during training and leverage the sparsity of wavelets to compress our model after training. Our goal is to provide a method that can be run on using single NVIDIA RTX 3090 GPU without custom CUDA code and to facilitate compression over bandlimited networks. Our pipeline decomposes a 4-D scene into a set of six (2-D) grids, similar to K-Planes [8], and uses the 2-D inverse discrete wavelet transform (IDWT) to recover these feature planes from a wavelet-based 2-D grid representation. However, this is **not** sufficient as the space-time plane features are not directly interpretable using the IDWT.

Plane-based NeRFs require a feature fusion process for final rendering [3, 9, 21]. For instance, Fridovich-Keil *et al.* [8] propose an element-wise feature factorization scheme, for features sampled from 6 orthogonal planes, reasoning that this can localize fused features. However, this approach does not fully localize features in 4-D space due to the influence of the multiplicative-0 identity, whereby for a given volume a single zero-valued feature will negate all other feature samples. Therefore, we propose a new strategy that enhances signal localization in 4-D by ensuring that space-time features sampled from the xt, yt, zt planes agree on a 0-valued fused feature. This approach improves temporal rendering details, notably in regions of high frequency and occlusion.

In the above context, our main contributions are:

1. A novel dynamic NeRF method that leverages space-time features recovered from the wavelet coefficient planes using the IDWT. Our approach (i) preserves the simplicity of the wavelet planes initialisation strategy, leading to more robust results, and (ii) naturally conditions wavelet planes to be sparse, necessary for achieving high quality and higher compression rates.

2. A novel wavelet-based compression scheme, which is accomplished without involving additional learnable parameters thus mitigating delays in training time and unnecessary computation.

3. A novel time sparsity (TS) regularizer. This works directly on the wavelet coefficients planes and avoids additional constraints laid out.

4. A novel feature fusion scheme, Zero-Agreement Masked (ZAM) fusion, that corrects localization errors arising from an element-wise multiplicative fusion scheme when rendering a novel view at specific time frames. This aims to promote high frequency details and visual quality for occlusions.

2 Related Work

Dynamic NeRFs. Existing methods for representing 3-D volumes in time can be divided into four main classes:

1. *Jointly learning a 3-D “canonical” (static) and 3-D deformation field.* This anchors the canonical field to a point in time, typically $t = 0$ s, where the deformation field linearly shifts canonical field volumes in space, conditioned on time, as proposed in D-NeRF [18] and Dy-NeRF [13]. It disentangles time-conditioned spatial features in a way that preserves volumetric consistency. However, they are not capable of discovering view-dependant effects under motion. NeRF-DS [27] addresses this by conditioning color features on surface position and orientation. Unfortunately, this approach still fails to adapt to temporal changes in scene topology.

2. *Decomposing 4-D into representational components*, such as matrix-vectors and planes. This approach was introduced in Tensor4D [21], which offers a 9-plane candecomp/parafac [4, 11] /matrix-matrix (MM) decomposition. Subsequently, K-Planes [8] and HexPlanes [3] proposed a 6-plane and 6-plane+6-vector decomposition, respectively, along with various feature-plane fusion schemes. HexPlanes uses a multiplicative-additive approach similar to Tensor4D, while K-Planes demonstrates that a purely multiplicative approach is preferred over an additive approach.

3. *Using static representations as a set of key-frames.* This approach relies on the robustness and compactness of static NeRF representations, along with the effectiveness of a key-frame interpolation strategy. NeRFPlayer [24] decomposes features into static, deforming and new areas, where the latter is used to represent temporal changes that occur after the first key frame, such as water gradually mixing with coffee. HyperReel [1] employs a hierarchical key-frame interpolation strategy that is compact and fast as a result of using TensoRF [5] for modelling each key-frame. However, it is limited by computational requirements needed to load the model. There is also an overlap with approach (2), as HumanRF [12] utilizes a key-framed MM decomposition for dynamic human modelling; storing and selecting a set of space-only (static) feature planes for at each time frame.

4. *Directly learning a 4-D field conditioned on time.* This groups the remaining work. DynIBaR [14] proposes a novel ray-conditioning scheme for dynamic videos, where features in each frame are conditioned on the predicted features of

surrounding frames. V4D [10] employs a texture driven, time-conditioned, voxel-based model where pixel-level refinement and a conditional positional encoder are used to handle over-smoothing caused by the total variation regularizer.

Each approach offers benefits and drawbacks. For instance, using MLPs results in small model size but is limited by long optimization times [13, 18]. Whereas explicit approaches, like K-Planes, offer faster optimization but require significantly more storage. As a plane-based approach our method is fast, yet not limited by model size. Our model is also capable of running synthetic and real scenes on a single GPU, which is not possible with the current SotA.

Wavelet NeRFs. Using wavelets to model static scenes is a recent development which has demonstrated the ability to enhance the compactness of existing representations [19, 20, 26]. WIRE [20] proposed better-suited activation functions for implicit neural representations and achieves a reduction of $p/\sqrt{2}$ w.r.t the number of trainable parameters by proposing a complex Gabor wavelet activation. This can be employed for a range of vision tasks such as image super resolution and NeRF synthesis. The MWT method [19] introduced learning a tri-plane decomposed wavelet-based representation for static scenes. To improve compression, a binary mask for each plane is learnt to exploit the sparsity of their tri-plane representation, which reduces the model size significantly. However this approach proves ineffective with dynamic NeRFs, as challenges arise from interpreting space-time features, usually 1-valued. A plane consisting mainly of 1-valued features will not produce a sparse wavelet representation, posing a quality and compression issue.

In this paper we introduce the first wavelet-based approach for modelling 4-D volumes. Our approach preserves sparsity in all dimensions. Unlike MWT, where compression relies on the training algorithm and the ability to decode the binary bit mask, our approach does not require learning additional parameters for our compression scheme. It is explicit and only needs to be executed once, after training.

3 WavePlanes

The model pipeline for WavePlanes is shown in Fig. 2. The representation is stored as a set of 2-D wavelet coefficients, Ω_c^s where $s \in [0, 1, \dots, N]$ denotes the wavelet level (scale) and $c \in C = \{xy, xz, yz, xt, yt, zt\}$ identifies the orientation of the plane in global space. Ω_c^s is encoded using the IDWT into a fine feature plane, \mathbf{P}_c^r where $r = 0$, and a coarse feature plane where $r = 1$, as shown in Fig. 2 (a). This is accomplished by performing the IDWT twice with the full set (all N -levels) and a reduced set ($N - 1$ levels) of wavelet coefficients, respectively.

To construct and render a 3-D volumetric model of the 4-D decomposed feature space we project a normalized 4-D sample, $\mathbf{q} = [x, y, z, t]$, onto each feature plane \mathbf{P}_c^r and bi-linearly interpolate using $f(\mathbf{q})_c^r = \psi(\mathbf{P}_c^r, \pi_c(\mathbf{q}))$, where π_c denotes the planar projection and ψ denotes the bi-linear interpolation of a projected point on a 2-D grid, Fig. 2 (b). Subsequently, the features for \mathbf{q} are fused, linearly decoded into color and density values and rendered w.r.t \mathbf{q} 's

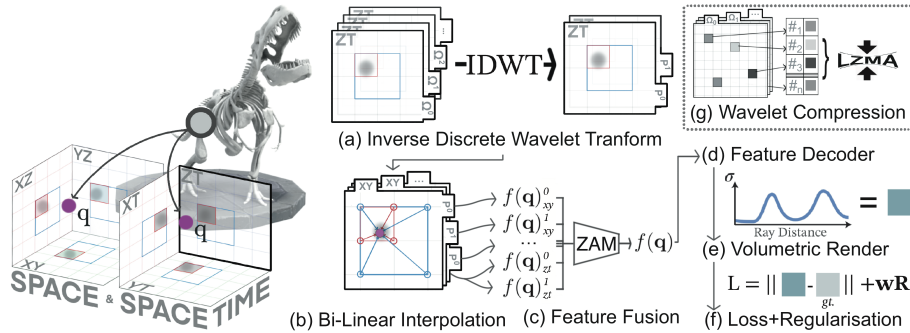


Fig. 2: Model Pipeline: (a) N-level wavelet planes are transformed using the IDWT into feature planes. (b) 4-D samples are projected onto each plane and bi-linearly interpolated over multiple scales. (c) Volumetric features are recovered by fusing the space-only and space-time features. (d) Features are linearly decoded into color and density values. (e) A 2-D pixel is rendered from the 3-D volume using the NeRF volumetric rendering function. (f) A loss and weighted regularization is used for training. (g) *After training* we compress non-zero wavelet coefficients

position along a camera ray using the classical NeRF equation [16], Fig. 2 (c-e) respectively. Finally, a loss and weighted regularization is applied to constrain the NeRF, Fig. 2 (f).

After training, we filter out zero-valued wavelet coefficients and store the non-zero coefficients and their locations in Ω_c^s . We then apply further lossless compression to reduce to model size - ready for any data transmission task. This is shown in Fig. 2 (g).

3.1 Feature Plane Reconstruction

The 2-D wavelet coefficient planes are separated into *father* wavelet coefficients, representing a low resolution approximation of the feature planes \mathbf{P}_c^0 , and *mother* wavelets coefficients, responsible for modelling fine details at various frequency bands. We refer to the father wavelet coefficients as $\Omega_c^{[s=0]} \in \mathcal{R}^{B \times H/2^N \times W/2^N}$, where B is the feature length, (H, W) is the desired height and width of the reconstructed feature plane and 2^N is a down-sampling factor involved in wavelet decomposition. The mother wavelet coefficients are defined as $\Omega_c^{[s>0]} \in \mathcal{R}^{B \times 3 \times H/s' \times W/s'}$, where 3 indicates the number of filters¹ and $s' = 2^{N-s}$ allows for down-sampling where the lowest and highest frequency planes will have size $(H/2^N, W/2^N)$ and $(H/2, W/2)$ respectively. Hence, for a wavelet decomposition level of 2, $N = 2$ and $s \in [0, 1, 2]$.

To reconstruct the feature planes we use Eq. (1). To avoid vanishing gradients for high-frequency coefficients during the IDWT, we apply the frequency-based scaling factor to each plane, denoted by $\mathbf{k} \odot \Omega_c$ as suggested in [19], where we

¹ Horizontal (LH), vertical (HL) and diagonal (HH) filters.

select $\mathbf{k} = [1, \frac{2}{5}, \frac{1}{5}]$ (please refer to the Supplementary Materials).

$$P_c^s(\Omega_c|s) \begin{cases} \text{IDWT}(\mathbf{k} \odot \Omega_c^{[0:s]}), & \text{if } c \in [xy, xz, yz], \\ \text{IDWT}(\mathbf{k} \odot \Omega_c^{[0:s]}) + 1, & \text{otherwise,} \end{cases} \quad (1)$$

Here, we introduce the +1 term which shifts the space-time features towards 1. This ensures that features sampled from the space-time planes, $c = c_t \in C_t = \{xt, yt, zt\}$ are initialized and regularized towards 1. The +1 term preserves sparsity in the wavelet representation. Thus, this maximises the likelihood of 1-valued space-time features, interpreted as empty static space during feature fusion. This significantly improves performance as scenes are typically full of empty space. Additionally, it simplifies model initialization by allowing all wavelet coefficients to start as 0-valued.

The resulting sparsity of wavelet coefficients also benefits our compression scheme, discussed in Sec. 3.3.

3.2 Feature Fusion with Zero-Agreement Mask (ZAM)

Prior work has proposed the Hadamard Product (HP) (element-wise multiplication) [8] in Eq. (2) over an additive approach:

$$f(\mathbf{q}) = \llbracket \prod_{c \in C} f_c^r(\mathbf{q}) \rrbracket^{r \in S} \quad (2)$$

where \prod applies the HP operator fusing plane features and $\llbracket \cdot \rrbracket$ represents a concatenation across scales. HP multiplies features sampled from the orthogonal planes to produce a localized signal [8]. However this breaks down when we consider the (globally) destructive nature of 0-valued features in Eq. (2). For example, when $f(\mathbf{q})_{xy}^0 = 0$, $f(\mathbf{q})$ is zero regardless of the z and t components in \mathbf{q} . This is not significant for 0-valued space-only features as this can indicate undisturbed vector volumes (*e.g.* along the z -axis). However, 0-valued space-time features operate under a single spatial axis so will affect larger volumes of space, *e.g.* when $f(\mathbf{q})_{xt}^0 = 0$, y and z axis' will be affected.

With K-Planes, this issue is avoided by regularizing the space-time features towards 1, which in turn leverages the multiplicative-1 identity (when $f(\mathbf{q})_{c_t}^r = 1$ for all c_t) - a useful but simple tool for separating static and dynamic volumes in a scene. However, in practice a large share of dynamic features are still present on the space-only (static) planes², leading to a temporal loss in visual quality in regions containing high frequency occlusions (*e.g.* the T-Rex teeth and tail in Fig. 1).

Consequently, we propose the **zero-agreement masked** (ZAM) fusion in Eq. (3), where a sum of 0 results in the multiplicative-0 identity only when all space-time features agree and the 1/3 factor ensures that when all space-time features are 1 the sum is also 1 - retaining the separability of static and dynamic

² A visual example is provided in the Supplementary Materials.

volumes. Conditioning all space-time features to agree on a 0-valued, $f(\mathbf{q})$, allows for the possibility of localized destruction resulting in a reduction of noise around high-frequency occlusions.

$$f(\mathbf{q}) = \llbracket \frac{1}{3} \sum_{c_t \in C_t} f_{c_t}^r(\mathbf{q}) \cdot \prod_{c \in C} f_c^r(\mathbf{q}) \rrbracket^{r \in S} \quad (3)$$

3.3 Compressing Wavelets with Hash Maps

A benefit of using wavelets is the ability to compress representations by relying on the tendency of coefficients to be zero. Unlike other plane-based models, this is true for all of our planes and is possible thanks to the condition proposed in Eq. (1).

To compress the wavelet representation, we first filter out 0-valued wavelet coefficients using hard thresholding and store the non-zero coefficients and their individual locations on each wavelet plane, Ω_c^s . Next, we apply lossless compression to further reduce the final size of the model. Conversely, to load the model from the compressed representations we initialize the wavelet planes with zero-values and move the non-zero coefficient back to their original locations.

Why not compress the feature planes? While there are certainly fewer feature planes than wavelet coefficient planes, the majority of non-zero coefficients are concentrated at the lowest resolution father wavelet planes, which are 2^N smaller than the highest resolution feature planes. Additionally, the highest resolution mother wavelet planes are $1/4$ the size of the feature planes, and are the sparsest representation in the set of mother wavelet coefficients.

Why hard thresholding? Modifying non-zero coefficients (even slightly), for instance with soft thresholding, results in visually incomprehensible renders as the linear decoder is sensitive to minor changes in the feature space. Also, filtering out near-zero coefficients can reduce noise and promote sparsity.

Why Hash Maps? This allows for storing and loading non-zero wavelet coefficients efficiently, and supports further compression using lossless compression schemes. Here, we selected the Lempel–Ziv–Markov chain (LZMA) scheme as it provides the best compression (see ablation experiments).

3.4 Optimization

Regularization. For dynamic scenes, we use three regularizers: total variation (TV), spatial smoothness in time (SST) and time sparsity (TS). TV regularization, in Eq. (4), is used for static scenes in Plenoxels [9] and TensorRF [5] and recently for dynamic scenes in K-Planes and HexPlanes.

$$\mathcal{L}_{TV}(\mathbf{P}) = \frac{1}{|C|n^2} \sum_{c,i,j} (\|\mathbf{P}_c^{i,j} - \mathbf{P}_c^{i-1,j}\|_2^2 + \|\mathbf{P}_c^{i,j} - \mathbf{P}_c^{i,j-1}\|_2^2) \quad (4)$$

The SST regularizer, in Eq. (5), represents the 1-D Laplacian approximation of the second derivatives of the spatial components for each time-plane. Rather

than smoothing along the time-axis as proposed by Fridovich-Keil *et al.* [8], smoothing along the spatial axis preserve details and avoids over smoothing in the presence of fast motion, leading to better perceptual results. Please refer to the supplementary materials for an ablation study.

$$\mathcal{L}_{SST} = \frac{1}{|C|n^2} \sum_{c,i,t} \|\mathbf{P}_c^{i-1,t} - 2\mathbf{P}_c^{i,t} + \mathbf{P}_c^{i+1,t}\|_2^2 \quad (5)$$

TS regularization, proposed in Eq. (6), uses ℓ_1 -norm to promote sparsity, maximizing the number of zero-valued space-time wavelet coefficients. This pairs well with our compression scheme as it directly maximizes the sparsity of $\Omega_{c_t}^s$. This also avoids further computation involved with the sparse transients regularizer proposed in [8] as we no longer require additional terms.

$$\mathcal{L}_{TS} = \sum_{c_t \in C_t} \|\Omega_{c_t}\|_1 \quad (6)$$

Feature decoder with learned color basis. To decode volumetric features into color and density values Wizarwongsa *et al.* [25] propose a per-scene learned color basis (also used in K-Planes), where features are treated as coefficients for a linear decoder. We utilize the same approach where a basis is learnt using a tiny fully-fused MLP [17]. This maps the viewing direction of a camera ray \mathbf{d} to red, green and blue basis vectors, $b_i(\mathbf{d})$ for $i \in \{R, G, B\}$. An additional density basis is learnt and left independent of viewing direction. Subsequently, color and density values are recovered by applying the dot product between basis vectors $b_i(\mathbf{d})$ and the fused feature $f(\mathbf{q})$.

Proposal Sampling Network. Mip-NeRF 360 [2] introduces proposal sampling as a trainable method to improve the sampling of spatial features by learning a probability density function of dense regions of space; trained using a histogram loss function. We employ a two-stage proposal sampling strategy, that uses two smaller versions of WavePlanes.

Importance Sampling based on temporal differences (IST) is proposed in DyNeRF [13] to handle the real dynamic DyNeRF data set. Rays are sampled in relation to their maximum color variance, thus higher sampling is attributed to 4-D volumes that are assumed to be dynamic. We follow the same strategy proposed in [8], whereby we sample rays uniformly for the first half of training and then apply the IST strategy.

3.5 Implementation

Our implementation is a fork off the K-Planes repository. To implement the wavelet functionality we use the *pytorch_wavelets* library [6]. To boost training speed we cache (on the GPU) the resulting feature planes, \mathbf{P}_c^s , at the start of every epoch to avoid re-processing the IDWT during regularization. This significantly reduces training time although it does increase memory consumption, as shown in Tab. 1. Compared to K-Planes the GPU utilization is lower. This is important as utilization ultimately limits our ability to run K-Planes on larger data sets with our available hardware.

Table 1: Computational comparisons of our model with and without caching the wavelet representation. Further comparison with K-Planes is provided and both models use HP fusion for fair comparison. *Mem.* is the GPU memory. *Util.* is the GPU utilization. *Time* is the training time. “-” indicates it did not run on our hardware

Method	D-NeRF data set [18]			DyNeRF data set [13]		
	Mem. ↓	Util. ↓	Time ↓	Mem. ↓	Util. ↓	Time ↓
K-Planes [8]	7.0 GB	86%	59 mins	-	-	-
Ours	7.7 GB	79%	72 mins	9.7 GB	89%	510 mins
Ours without Caching	7.4 GB	70%	120 mins	9.1 GB	82%	690 mins

4 Results

We employ a 4k batch size and the same scene bounding boxes used in K-Planes [8] for fair comparison. For synthetic scenes, we select a spatial resolution of $H = W = 256$ for high-complexity scenes³ and 128 for low-complexity scenes. This reduces memory consumption and training time while producing results comparable to other models with resolutions up to 512. Additionally, for all experiments, we evaluate our ZAM approach with feature length $B = 64$, using PSNR and SSIM, as shown in Tab. 2. Quantitative (objective metric) results for the HP approach are provided in the supplementary materials and show similar overall performance. Note that we did not retrain existing models; all results were taken from the original papers. In the ablation study, we further separate the PSNR evaluation for foreground and background renders. This reduces ambiguity in image-quality assessment metrics, which can exhibit bias towards large white backgrounds for synthetic scenes. The foreground and background are separated using the alpha mask of RGBA image data sets. Then morphological dilation is applied to include noisy foreground artifacts in foreground evaluations.

All tests were performed using a 24GB NVIDIA RTX 3090 GPU. For LLFF and D-NeRF data sets we used 32GB of RAM whereas DyNeRF required 98GB of RAM. For most data sets this is not an issue. However, for the DyNeRF data set [13] we are unable to pre-generate IST weights with the usual $2\times$ down sampling, due to limited RAM. Hence, we down sampled by $8\times$ during IST weight generation and by $2\times$ during training; allowing us to demonstrate our model’s ability to synthesize real dynamic scenes.

4.1 Real Static Scenes

Although our WavePlanes is purposed for dynamic NeRFs, we tested it on a real multi-view static LLFF data set [15] to investigate strengths and limitations. Most methods designed for dynamic scenes often fail to produce results for static scenes as they are challenging to simplify for 3-D scenes. Each scene contains 20-60 images and is down sampled to 1008×756 pixels. In this experiment WavePlanes is reduced to a tri-plane model, using HP fusion. While it

³ Containing high frequency features and occlusions.

Table 2: Average novel view synthesis results. *Partial* indicates a subset of the data set. * indicates the methods proposed specifically for static NeRF

	PSNR \uparrow		SSIM \uparrow	# Params \downarrow	Average Size \downarrow
	Full	Partial			
Real static LLFF scenes [15]					
Plenoxels* [9]	26.29	28.84	0.839	500M	-
Masked Wavelets* (small) [19]	26.25	29.05	-	-	3.2MB
Masked Wavelets* (large) [19]	26.54	29.42	-	-	7.4MB
K-Planes (explicit) [8]	26.78	29.75	0.841	19M	\sim 100MB
Ours	26.10	29.30	0.823	51M	93MB
Real dynamic DyNeRF scenes [13]					
HexPlanes [3]	31.71	-	-	-	\sim 200MB
K-Planes (explicit) [8]	31.30	-	0.963	51M	250MB
K-Planes (hybrid) [8]	31.92	-	0.966	27M	250MB
Ours	30.14	-	0.926	67M	58MB
Synthetic dynamic D-NeRF assets [18]					
D-NeRF [18]	29.67	26.14	0.95	1-3M	13MB
V4D [10]	33.72	29.06	0.97	275M	377MB
TiNeuVox-S [7]	30.75	27.10	0.96	-	8MB
TiNeuVox-B [7]	32.67	28.63	0.97	-	48MB
HexPlanes [3]	31.04	26.71	-	-	\sim 200MB
K-Planes (explicit) [8]	31.05	27.45	0.97	37M	\sim 200MB
K-Planes (hybrid) [8]	31.61	27.66	0.97	37M	\sim 200MB
Ours	30.51	27.49	0.97	16M	10MB

performs satisfactorily over the full data set, WavePlanes demonstrates competitive performance on scenes containing >35 training images, indicated by the **partial results** in Tab. 2. Visually, WavePlanes is better at dealing with edges and is capable of modelling high frequency details, *e.g.* the rib-cage in Fig. 3. The WavePlanes result also exhibits better texture detail with fewer ghosting artifacts compared to that of K-planes, demonstrated by the petal edges in Fig. 3.

4.2 Dynamic Scenes

Real multi-view scenes. The DyNeRF data set [13] is used to test our model’s ability to perform novel view synthesis on forward-facing, multi-view (19-21 cameras), real dynamic scenes lasting 10 seconds at 30FPS. The scenes contain different indoor lighting set-ups with a large variation of textures and materials. For this test, we use a temporal resolution of $W = 150$ (i.e. half the number of frames). Quantitative results in Tab. 2 indicate desirable performance for our method, considering the reduced quality of the IST weight pre-generation. As shown in Fig. 4, WavePlanes performs novel view synthesis well and shows sharper edges and less noise on a number of objects in the scene, *e.g.* the pattern on the uncooked salmon is clearer whilst those of K-Planes are smoothed out. This is notably accomplished with a memory budget at least $4\times$ smaller than

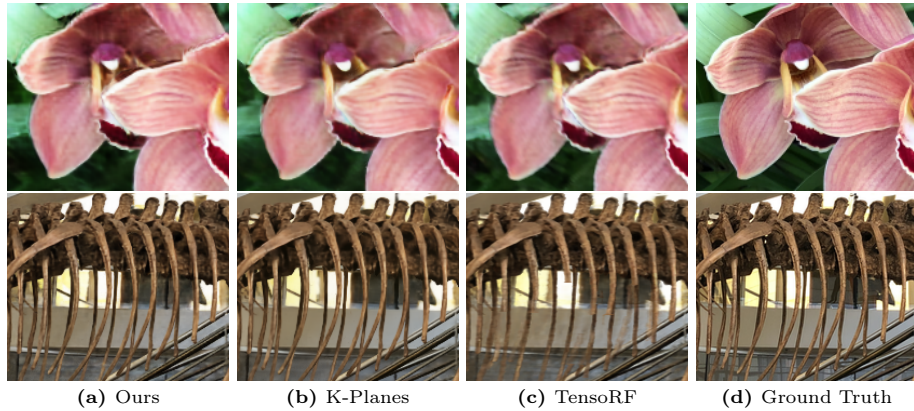


Fig. 3: Zoomed visual comparison of real static scene renders. Demonstrating WavePlanes ability to model static scenes

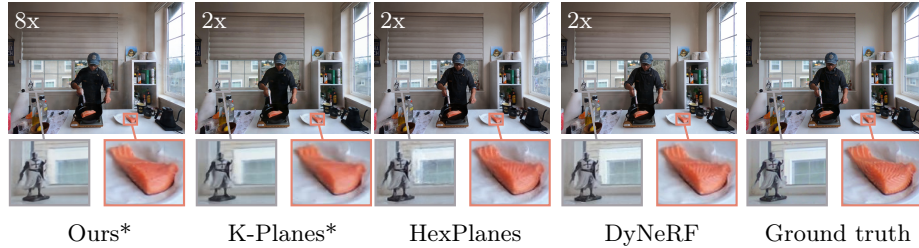


Fig. 4: Qualitative real video results. WavePlanes can synthesize real objects to an acceptable standard. *Trained on the first 10/40 seconds

other plane-based methods and is run on a single GPU rather than with high performance computing resources.

Synthetic monocular scenes. The D-NeRF data set [18] was used to perform novel view synthesis on low and high complexity synthetic object animations. These were captured using monocular “teleporting” cameras rotated at 360° and contain 50-200 training frames that are down sampled to 400×400 pixels. For this experiment, the resolution of the time axis for space-time planes is equivalent to the number of training images. WavePlanes performs particularly well on scenes containing a high amount of occlusion while being significantly more compact and small in size. This is indicated by the **partial results** in Tab. 2 that comprises the Lego, T-Rex and Hell Warrior scenes. The visual results in Fig. 1 show that WavePlanes achieves cleaner results than K-Planes and produces better detail in high frequency areas than K-Planes and TiNeuVox, *e.g.* around the T-Rex’s tail and jaw. Compared with other small dynamic NeRFs our method produces significantly better visual results on complex scenes, *e.g.* the Lego scene in Fig. 5. The Hook scene in Fig. 5 also shows a common failure case for most models. Our method smooths high-frequency errors found in K-Planes, avoiding temporal jitter effects associated with high frequency errors,

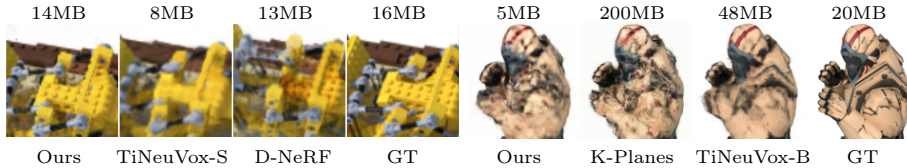


Fig. 5: Visual comparisons of the Lego (**left**) and Hook (**right**) D-NeRF scene [18] where the ground truth (GT) size is for the data set

Table 3: Quantitative results for propose feature fusion schemes. We compare quality and training time to other plane-based models

	T-Rex D-NeRF [18]				Flame Salmon DyNeRF [13]			
	PSNR \uparrow			SSIM \uparrow	Time \downarrow	PSNR \uparrow	SSIM \uparrow	Time \downarrow
	Whole	Front	Back					
K-Planes	31.28	-	-	0.980	58min	28.71	0.942	222min
HexPlanes	30.67	-	-	-	11min	29.47	-	720min
HP	31.40	20.73	77.18	0.978	72min	27.31	0.893	510min
ZAM	31.44	20.78	75.18	0.978	76min	28.25	0.900	530min

making the visual result more appealing, *e.g.*, the mouth guard and shoulder of the Hook character.

4.3 Feature Fusion

Results provided in Tab. 3 and Fig. 6 demonstrate the effectiveness of the proposed feature fusion schemes on the D-NeRF data set. Despite the difference in IST down sampling, ZAM provides decent objective results for the real scene. Notably, we find the ZAM method is more capable of dealing with high frequency occlusion artifacts, for example comparing the ribcage and arm in Fig. 6, indicating that our ambition to better preserve details for high frequency features is met.

4.4 Ablation Study

We perform an ablation study using the D-NeRF synthetic data set [18]. Please refer to the supplementary materials for further details and more results.

Wavelet family. Tab. 4 compares different wavelet functions with varying degrees of regularity. Regularity indicates the number of continuous derivatives that wavelet function has and is tied to the number of vanishing moments, denoted by the M in “DbM”, “CoifM”, etc. For wavelets with less regularity (*e.g.* the Haar wavelet) our method performs badly on foreground predictions. Wavelets with higher regularity are also negligibly slower. However, we find that the Coif4 wavelet is an exception as it is performant yet slightly slower (by $< 7\%$). This is likely because it has a larger filter length, of $6M$, compared with other functions such as DbM with length $2M$. This also leads to better

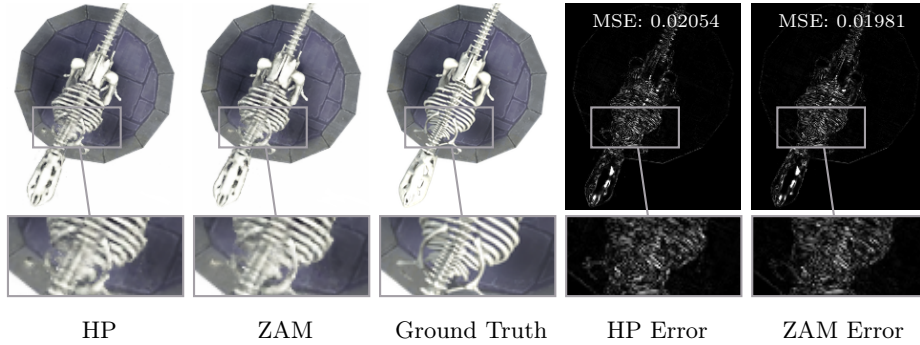


Fig. 6: Qualitative feature fusion results

Table 4: **Left:** Comparing the quality of various wavelet families. **Right:** Comparing N-levels of wavelet decomposition

Family	PSNR \uparrow			SSIM \uparrow	N-Level	PSNR \uparrow			Time \downarrow	
	Whole	Front	Back			Whole	Front	Back		
Haar	31.33	20.55	73.15	0.9779		30k iterations				
Coif2	31.17	20.50	72.66	0.9783	2	31.44	20.78	75.81	0.9783	76 mins
Coif4	31.44	20.78	75.81	0.9783	3	31.20	20.54	74.29	0.9772	80 mins
Bior1.3	31.26	20.57	73.48	0.9779	4	30.28	19.61	71.06	0.9742	102 mins
Bior4.4	31.26	20.60	72.56	0.9781		60k iterations				
Db2	31.14	20.48	74.08	0.9780	3	31.75	21.09	74.72	0.9800	176 mins
Db6	31.36	20.69	75.30	0.9781	4	31.11	20.45	76.32	0.9782	205 mins

results hence our selection of the Coif4 wavelet for our final model. Overall, the results indicate that orthogonality and symmetry have little importance, whereas the function’s shape, regularity and filter length impacts performance the most. Similar conclusions were found for low-bit rate wavelet coding tasks [23], which may suggest that this is shared characteristic of low-resolution image tasks, such modelling dynamic scenes using low resolution (400×400 pixel) images.

Wavelet decomposition level. In Tab. 4 we compare the number of wavelet levels for the main WavePlane field for a fixed number of training steps (30k). Two levels gives the best results in the shortest time. More levels of decomposition means more coefficients, which in turn impacts computation and rendering time significantly. The convergence associated with higher levels of wavelet decomposition is also slower. For instance, a level of 3 trained for 60k steps will produce significantly better results however requires more than double the training time. Considering our goal is to prioritize computation and provide faster training times, we opt for the 2 level wavelet decomposition.

Compression Scheme. There are two parameters to evaluate for our compression scheme. The first compares the additional lossless serial compression on the Hash Map representation of our model and the second compares the use of hard thresholding and the fixed threshold, left and right side in Tab. 5 respectively. This leads to our choice of LZMA for our compression scheme as well as

Table 5: Left: Comparing final model size (in MB) with different lossless compression schemes where *None* indicates no additional compression. **Right:** Comparing the hard threshold value against the original results

Scene	Hash Map + Compression					Hard Threshold				
	None	Pickle	GZIP	BZ2	LZMA	Original	0.4	0.2	0.1	
T-Rex	82 MB	61 MB	24 MB	20 MB	18 MB	PSNR	30.441	31.050	31.415	31.447
Balls	36 MB	10 MB	4 MB	3 MB	3 MB	PSNR-F	20.775	20.383	20.743	20.781
Lego	67 MB	47 MB	18 MB	15 MB	14 MB	PSNR-B	75.179	73.897	75.844	75.698
Mutant	36 MB	20 MB	8 MB	7 MB	6 MB	SSIM	0.9783	0.9760	0.9781	0.9783

the fixed threshold of 0.1. Interestingly we find that applying hard thresholding slightly improves PSNR results compared to when hard thresholding is not used.

5 Conclusion and Future Work

Conclusion. We propose WavePlanes, the first wavelet-based approach for modelling dynamic NeRFs. We show that our model can synthesize various scenes without the need for high performance computing resources, while producing competitive objective results and perceptually pleasing visual results. By exploiting the characteristics of the wavelet representation, our novel compression scheme reduces the final model size by up to $15\times$ compared to other plane-based models without significantly impacting training time or performance.

Future work. Plane-based approaches are currently limited in their ability to model objects outside of the predefined bounding box [8, 19, 21]. Future work should therefore model the out-of-bounds scene with a HDRI-style mapping, similar to what was proposed for NeRF++ [28].

Additionally, using discrete grids with a fixed temporal resolution makes it challenging to model fast motion without introducing some degree of temporal uncertainty (noise). This limitation is shared by current dynamic plane-based models. However, the results from our compression scheme indicate that the high pass filter applied to our wavelet representation may be useful for denoising. Consequently, a more sophisticated approach could be explored to correct regions of space-time affected by high motion noise. For instance, by classifying wavelet features a band pass filter could be used to contract features dispersed around a class means. Filtering non-zero coefficients would also lead to better compression as more values would be repeated. This may alleviate limitations in our compression scheme when a scene contains little empty space, as is the case for numerous LLFF scenes.

References

1. Attal, B., Huang, J.B., Richardt, C., Zollhoefer, M., Kopf, J., O’Toole, M., Kim, C.: Hyperreel: High-fidelity 6-dof video with ray-conditioned sampling. In: Proceedings

- of the IEEE/CVF Conference on Computer Vision and Pattern Recognition. pp. 16610–16620 (2023) [3](#)
2. Barron, J.T., Mildenhall, B., Verbin, D., Srinivasan, P.P., Hedman, P.: Mip-nerf 360: Unbounded anti-aliased neural radiance fields. In: Proceedings of the IEEE/CVF Conference on Computer Vision and Pattern Recognition. pp. 5470–5479 (2022) [8](#)
 3. Cao, A., Johnson, J.: Hexplane: A fast representation for dynamic scenes. In: Proceedings of the IEEE/CVF Conference on Computer Vision and Pattern Recognition. pp. 130–141 (2023) [2](#), [3](#), [10](#)
 4. Carroll, J.D., Chang, J.J.: Analysis of individual differences in multidimensional scaling via an n-way generalization of “eckart-young” decomposition. *Psychometrika* **35**(3), 283–319 (1970) [3](#)
 5. Chen, A., Xu, Z., Geiger, A., Yu, J., Su, H.: Tensorf: Tensorial radiance fields. In: European Conference on Computer Vision. pp. 333–350. Springer (2022) [2](#), [3](#), [7](#)
 6. Cotter, F.: Uses of complex wavelets in deep convolutional neural networks. Ph.D. thesis (2020) [8](#)
 7. Fang, J., Yi, T., Wang, X., Xie, L., Zhang, X., Liu, W., Nießner, M., Tian, Q.: Fast dynamic radiance fields with time-aware neural voxels. In: SIGGRAPH Asia 2022 Conference Papers. pp. 1–9 (2022) [10](#)
 8. Fridovich-Keil, S., Meanti, G., Warburg, F.R., Recht, B., Kanazawa, A.: K-planes: Explicit radiance fields in space, time, and appearance. In: Proceedings of the IEEE/CVF Conference on Computer Vision and Pattern Recognition. pp. 12479–12488 (2023) [2](#), [3](#), [6](#), [8](#), [9](#), [10](#), [14](#)
 9. Fridovich-Keil, S., Yu, A., Tancik, M., Chen, Q., Recht, B., Kanazawa, A.: Plenoxels: Radiance fields without neural networks. In: Proceedings of the IEEE/CVF Conference on Computer Vision and Pattern Recognition. pp. 5501–5510 (2022) [2](#), [7](#), [10](#)
 10. Gan, W., Xu, H., Huang, Y., Chen, S., Yokoya, N.: V4d: Voxel for 4d novel view synthesis. *IEEE Transactions on Visualization and Computer Graphics* (2023) [4](#), [10](#)
 11. Harshman, R.A., et al.: Foundations of the parafac procedure: Models and conditions for an " explanatory " multimodal factor analysis (1970) [3](#)
 12. Işık, M., Rünz, M., Georgopoulos, M., Khakhulin, T., Starck, J., Agapito, L., Nießner, M.: Humanrf: High-fidelity neural radiance fields for humans in motion. arXiv preprint arXiv:2305.06356 (2023) [2](#), [3](#)
 13. Li, T., Slavcheva, M., Zollhoefer, M., Green, S., Lassner, C., Kim, C., Schmidt, T., Lovegrove, S., Goesele, M., Newcombe, R., et al.: Neural 3d video synthesis from multi-view video. In: Proceedings of the IEEE/CVF Conference on Computer Vision and Pattern Recognition. pp. 5521–5531 (2022) [3](#), [4](#), [8](#), [9](#), [10](#), [12](#)
 14. Li, Z., Wang, Q., Cole, F., Tucker, R., Snavely, N.: Dynibar: Neural dynamic image-based rendering. In: Proceedings of the IEEE/CVF Conference on Computer Vision and Pattern Recognition. pp. 4273–4284 (2023) [3](#)
 15. Mildenhall, B., Srinivasan, P.P., Ortiz-Cayon, R., Kalantari, N.K., Ramamoorthi, R., Ng, R., Kar, A.: Local light field fusion: Practical view synthesis with prescriptive sampling guidelines. *ACM Transactions on Graphics (TOG)* (2019) [9](#), [10](#)
 16. Mildenhall, B., Srinivasan, P.P., Tancik, M., Barron, J.T., Ramamoorthi, R., Ng, R.: Nerf: Representing scenes as neural radiance fields for view synthesis. *Communications of the ACM* **65**(1), 99–106 (2021) [5](#)
 17. Müller, T.: tiny-cuda-nn (4 2021), <https://github.com/NVlabs/tiny-cuda-nn> [8](#)

18. Pumarola, A., Corona, E., Pons-Moll, G., Moreno-Noguer, F.: D-nerf: Neural radiance fields for dynamic scenes. In: Proceedings of the IEEE/CVF Conference on Computer Vision and Pattern Recognition. pp. 10318–10327 (2021) [3](#), [4](#), [9](#), [10](#), [11](#), [12](#)
19. Rho, D., Lee, B., Nam, S., Lee, J.C., Ko, J.H., Park, E.: Masked wavelet representation for compact neural radiance fields. In: Proceedings of the IEEE/CVF Conference on Computer Vision and Pattern Recognition. pp. 20680–20690 (2023) [2](#), [4](#), [5](#), [10](#), [14](#)
20. Saragadam, V., LeJeune, D., Tan, J., Balakrishnan, G., Veeraraghavan, A., Baraniuk, R.G.: Wire: Wavelet implicit neural representations. In: Proceedings of the IEEE/CVF Conference on Computer Vision and Pattern Recognition. pp. 18507–18516 (2023) [4](#)
21. Shao, R., Zheng, Z., Tu, H., Liu, B., Zhang, H., Liu, Y.: Tensor4d: Efficient neural 4d decomposition for high-fidelity dynamic reconstruction and rendering. In: Proceedings of the IEEE/CVF Conference on Computer Vision and Pattern Recognition. pp. 16632–16642 (2023) [2](#), [3](#), [14](#)
22. Shue, J.R., Chan, E.R., Po, R., Ankner, Z., Wu, J., Wetzstein, G.: 3d neural field generation using triplane diffusion. In: Proceedings of the IEEE/CVF Conference on Computer Vision and Pattern Recognition. pp. 20875–20886 (2023) [2](#)
23. da Silva, E.A., Ghanbari, M.: On the performance of linear phase wavelet transforms in low bit-rate image coding. IEEE Transactions on Image Processing **5**(5), 689–704 (1996) [13](#)
24. Song, L., Chen, A., Li, Z., Chen, Z., Chen, L., Yuan, J., Xu, Y., Geiger, A.: Nerf-player: A streamable dynamic scene representation with decomposed neural radiance fields. IEEE Transactions on Visualization and Computer Graphics **29**(5), 2732–2742 (2023) [3](#)
25. Wizadwongsa, S., Phongthawee, P., Yenphraphai, J., Suwajanakorn, S.: Nex: Real-time view synthesis with neural basis expansion. In: Proceedings of the IEEE/CVF Conference on Computer Vision and Pattern Recognition. pp. 8534–8543 (2021) [8](#)
26. Xu, M., Zhan, F., Zhang, J., Yu, Y., Zhang, X., Theobalt, C., Shao, L., Lu, S.: Wavenerf: Wavelet-based generalizable neural radiance fields. arXiv preprint arXiv:2308.04826 (2023) [4](#)
27. Yan, Z., Li, C., Lee, G.H.: Nerf-ds: Neural radiance fields for dynamic specular objects. In: Proceedings of the IEEE/CVF Conference on Computer Vision and Pattern Recognition. pp. 8285–8295 (2023) [3](#)
28. Zhang, K., Riegler, G., Snavely, N., Koltun, V.: Nerf++: Analyzing and improving neural radiance fields. arXiv preprint arXiv:2010.07492 (2020) [14](#)